Progress Report: 9/15/94 - 9/14/95

Aeroelastic Analysis of Modern Complex Wings Using ENSAERO and NASTRAN*

Abstract

A process is presented by which static aeroelastic analysis is performed using Euler flow equations in conjunction with an advanced structural analysis tool, NASTRAN. The process deals with the interfacing of two separate codes in the fields of computational fluid dynamics (CFD) and computational structural dynamics (CSD). The process is demonstrated successfully on an F/A-18 Stabilator (horizontal tail).

Introduction

With advanced subsonic transports entering into the transonic regime and fighter aircraft being limited by aeroelastic phenomena, it is becoming increasingly important to perform static and dynamic aeroelastic analysis using highly accurate fluid and structural models. Recently, work has been done using advanced structural finite element wing-box models coupled with Euler flow equations, but the structural finite element model is a simple one.

There is a need to used highly detailed computation fluid dynamics (CFD) models coupled with highly detailed computational structural dynamics (CSD) models. Methods exist to solve each one independently, but not much work has been done coupling both highly accurate CSD and CFD models.

This paper presents a process by which a highly detailed CSD model is coupled with a highly detailed CFD model. The analysis of the CSD model is done using NASTRAN, while analysis of the CFD model is done using Euler flow equations in NASTD (an in-house McDonnell Douglas Aerospace East CFD code).

The aeroelastic process is broken down into the following steps:

1) Get CFD solution (possibly rigid steady state)
2) Calculate pressures at CFD grid points on the aerodynamic surface (Stabilator)
3) Map pressures to forces on structural grid
4) Obtain response of the structure

---

*NASA-Virginia Tech Consortium Agreement, NCC2-5097
This work was done in close association with Rudy Yurkovich of McDonnell Douglas Aerospace East during the first phase of the consortium agreement. As a part of the agreement, Manoj Bhardwaj spent the summer at McDonnell Douglas East.

5) Map displacements to the CFD grid points on the aerodynamic surface
6) Deform entire CFD grid
7) Repeat steps until convergence criteria is met

The above steps will sometimes be referred to later as one cycle. The above process will be demonstrated on an F/A-18 Stabilator (horizontal tail).

The CFD grid topology of the F/A-18 Stabilator can be seen in Figure 1, while a more accurate view will be seen later. The grid was divided into two zones so that the CFD portion of the process could be run using PVM to reduce computational time. The zone 1 grid contains the F/A-18 Stabilator, and the grid dimensions are 141 points around the perimeter of the airfoil, 69 points spanwise, and 61 points in the normal direction. Zone 2 looks like a rectangular box whose dimensions are 31 points running streamwise, 69 points running spanwise, and 121 points in the normal direction. The complete grid consists of more than 800,000 points, but the CFD code was run sequenced in each direction to reduce computational time. The k index for the tip of the Stabilator is 44, and the i index for the leading edge of the Stabilator is 71. Also, zone 2 matches with zone 1 as follows. The trailing edge of the Stabilator in zone 1 corresponds to i = 1 and i = 141, j = 1, and k = 1 to 69 (k = 44 is the Stabilator tip). These points are the same as i = 1, j = 61 , k = 1 to 69 in zone 2. A detailed grid is shown for the upper surface of the F/A-18 Stabilator in Figure 2.

The finite element model of the F/A-18 Stabilator is shown in Figure 3. The model consists of approximately 2000 nodes, 12000 d.o.f. This is the model used by NASTRAN to form the stiffness matrix. In the next few paragraphs, we will describe some of the steps involved in the aeroelastic process in more detail.

Step 1 involves getting a CFD solution. In this case, the rigid steady state solution was used. Next, the pressures were calculated using the CFD solution on the CFD grid.

Step 3 maps the pressures on the CFD grid to forces on the structural grid. This involves a pre-processed mapping. The mapping consists of the following information. For each CFD point (i,k) on the surface of the Stabilator, the area on which the pressure acts and unit normal is calculated. Now, the magnitude and direction of the force due to unit pressure is known. The next step is to find a structural triangle that surrounds the CFD point (i,k). This can be difficult due to the irregular grids of some structural models.

It is assumed that the structural grid is divided into an upper and lower surface structural grids with overlapping points possibly occurring at the leading and trailing edges and also at the tip. To find the structural triangle associated with the CFD grid point, the 20 closest structural nodes are found using the upper or lower surface structural grid depending on which surface the CFD point is located (Figure 4). Then all possible triangles using the 20 points are formed. Next, the triangles that do not contain the CFD point (i,k) as an interior point are eliminated (Figure 5). Then of the remaining triangles,

the largest vertex distance is measured for each triangle, where vertex distance is the distance between the structural node and CFD point (i,k). Finally, the triangle with the smallest largest vertex distance is chosen. The triangularization of the structural domain to the CFD domain for the F/A-18 Stabilator can be seen in Figure 6. Now that the structural triangle is known, the area coordinates of the CFD point are used to distribute the force to the nodes of the structural triangle. So for each CFD point (i,k), the necessary weight factors and destination nodes are known in the pre-processing stage as well as the direction of the application of the loads. As a side note, the 20 closest points can be changed to 25 closest points depending on the density of the structural grid.

Step 4 in the aeroelastic process is to solve the structural system of equations $[K]\{u_g\}=\{f\}$. The role of NASTRAN is a limited one, in that its only job is to produce the stiffness matrix in the pre-processing stage. In this example of the F/A-18 Stabilator, a reduced stiffness matrix is used.

At this point of the process, the pressures on the CFD grid have been mapped to forces on the structural grid, and the structural system of equations have been solved, and now $\{u_g\}$, the displacements are known.

The next step is to deform the CFD grid according to the displacements on the structural model. To interpolate the structural node displacements to displacements on the grid points on the aerodynamic surface, a surface spline by Harder and Desmarais is used. The remaining grid is deformed according to a cosine spacing function. The CFD grid is deformed only in the z-direction (normal). The in-plane displacements are neglected.

So to deform the surface grid, a surface spline technique was chosen. The surface spline system of equations become $[A]\{c\}=\{u_{spl}\}$. The [A] matrix is dependent on the coordinates of the spline points. Therefore, once the spline points are chosen, the [A] matrix can be generated in the pre-processing stage, and {c} is the vector of coefficients of the surface spline, while $\{u_{spl}\}$ are the displacements of the spline points.

The surface of the CFD grid which is deformed by the surface spline is shown in Figure 7. The red grid corresponds to zone 1 i = 1 to 141, j = 1 , k = 1 to 69 (k = 44 being the tip). The blue grid corresponds to zone 2, i = 1 to 31 , j = 61 , k = 1 to 69. The spline points were chosen from the surface grid as follows. Eighty six points were chosen from the surface of the structural finite element model shown in Figure 8. Looking at Figure 7, it is seen that more points are needed to ensure smoothness of the surface grid. So, additional spline points were chosen at the boundary of the surface grid. Three rows of points running streamwise near the spanwise tip (k = 67 to 69) in zone 1 and three rows of points near the streamwise tip (i = 29 to 31) in zone 2 were chosen as spline points with zero displacement enforced as can be seen in Figure 9. Once the spline points are chosen, the [A] matrix is generated and stored in the pre-processing stage.

Recalling, in the aeroelastic process, the displacements on the structural model have been calculated. The next step is to extract the spline point displacements $\{u_{spl}\}$ from the global displacements $\{u_g\}$. Once $\{u_{spl}\}$ are known, the system of equations $[A]\{c\}=\{u_{spl}\}$ are solved, and the coefficients of the surface spline are known.

The next step in the aeroelastic process is to deform the surface grid shown in Figure 7. This is done using the surface spline equation which is a function of the x and y coordinates of the point. This is done easily since the coefficients of the surface spline are now known.

Once the surface grid is deformed, the remaining grid (step 6) is deformed according to a cosine spacing function. It is enforced such that the outer boundaries corresponding to j = jmax in zone 1 and j = 1 and j = jmax in zone 2, do not move. So a spacing function that varies smoothly from 1 to 0 was is to deform the interior grid (Figure 10) which is itself a function of the normal index j. Once the surface grid is deformed, the remaining interior grid is deformed for each k = constant face. In order to prevent overlapping and crossed-sides of the CFD grid, a minimum spacing criteria is chosen, and the j = 26 face was found to meet the requirement. The points from j = 2 to 26 are deformed in each k = constant face the same amount as the j = 1 face. Then the spacing function is applied from j = 26 to jmax. This is done for zone 1 and zone 2. Zone 2 indices are different, but the same deformation procedure is used. Figure 11 shows the k = constant face. The red grid is the grid falling within the j = 26 surface, while the blue grid is the grid exterior to the j = 26 surface.

Finally, a convergence criteria is chosen. The L-2 norm of the CFD equations has to be converged and the Stabilator trailing edge tip displacement has to be converged. If not, then the process is repeated. Each time the process is repeated will be sometimes referred to as a cycle. Results are shown for the F/A-18 Stabilator at Mach 0.95, 1 degree angle of attack, at sea-level.

Results

Figure 12 shows the L-2 Norm of the zone 1 and zone 2 versus iteration. The rigid steady state solution was obtained after about 4000 iterations. The CFD grid was deformed and the CFD code was rerun starting with the previous step's CFD solution. Each time the grid was deformed and rerun is here referred to as a cycle. About 9 cycles were performed in the F/A-18 Stabilator example. The L-2 norm shows good convergence of the CFD equations. Also, the integrated loads and moments are also shown in Figures 13-16. The spikes in the figures corresponds to the aeroelastic cycles where the grid is being deformed. There was not any regular interval between cycles. The loads can be seen converging towards the final flexible Stabilator solution.

Figure 17 shows the displacements along the leading edge of the Stabilator. It can be seen that initially after the first cycle, the Stabilator deformed its greatest amount, and after cycle 2, it deformed its least amount. Figure 18 shows the convergence of the Stabilator tip airfoil section. This correlates well with Figure 17 also. The displacement

of the trailing edge of the Stabilator tip is plotted versus cycle number in Figure 19. It shows the convergence of the displacements.

The rigid and final flexible F/A-18 Stabilator is shown in Figure 20. The red solid figure is the rigid case, and the black grid lines are the deformed case. The deflections are scaled by a factor of 10 to help visualize the displacements.

Figure 21 shows the pressure coefficient variation on the upper surface of the rigid and flexible Stabilator. Not a big variation can be seen by the plot, but the shock location on the upper surface moves forward a little in the flexible Stabilator case. Figure 22 shows the Mach number variation on the upper surface of the rigid and flexible Stabilator. In this plot, it is easier to see that there is some change between the rigid and flexible cases, especially near the tip. There seems to be a discontinuity near the break of the trailing edge near the tip of the Stabilator in the flexible case. This is due to the fact that the CFD code was run sequenced, to reduce the computational time and effort.

Conclusions

The objective of this study was to create a process by which NASTRAN can be coupled with an advanced fluid model to perform aeroelastic analysis on highly detailed CFD and CSD models. The results show that this was achieved, but the process is somewhat problem dependent. The pressure to force mapping is a robust procedure since it requires only the structural node coordinates and CFD coordinates. It is independent of the type of elements used and does not require a rectangular domain. The displacement mapping is also good since it does not also require a rectangular domain and it's only dependent on the coordinates of the spline points chosen. It does require a user to choose spline points in advance and thus becomes problem dependent. Overall, the process has been successfully demonstrated on the F/A-18 Stabilator.

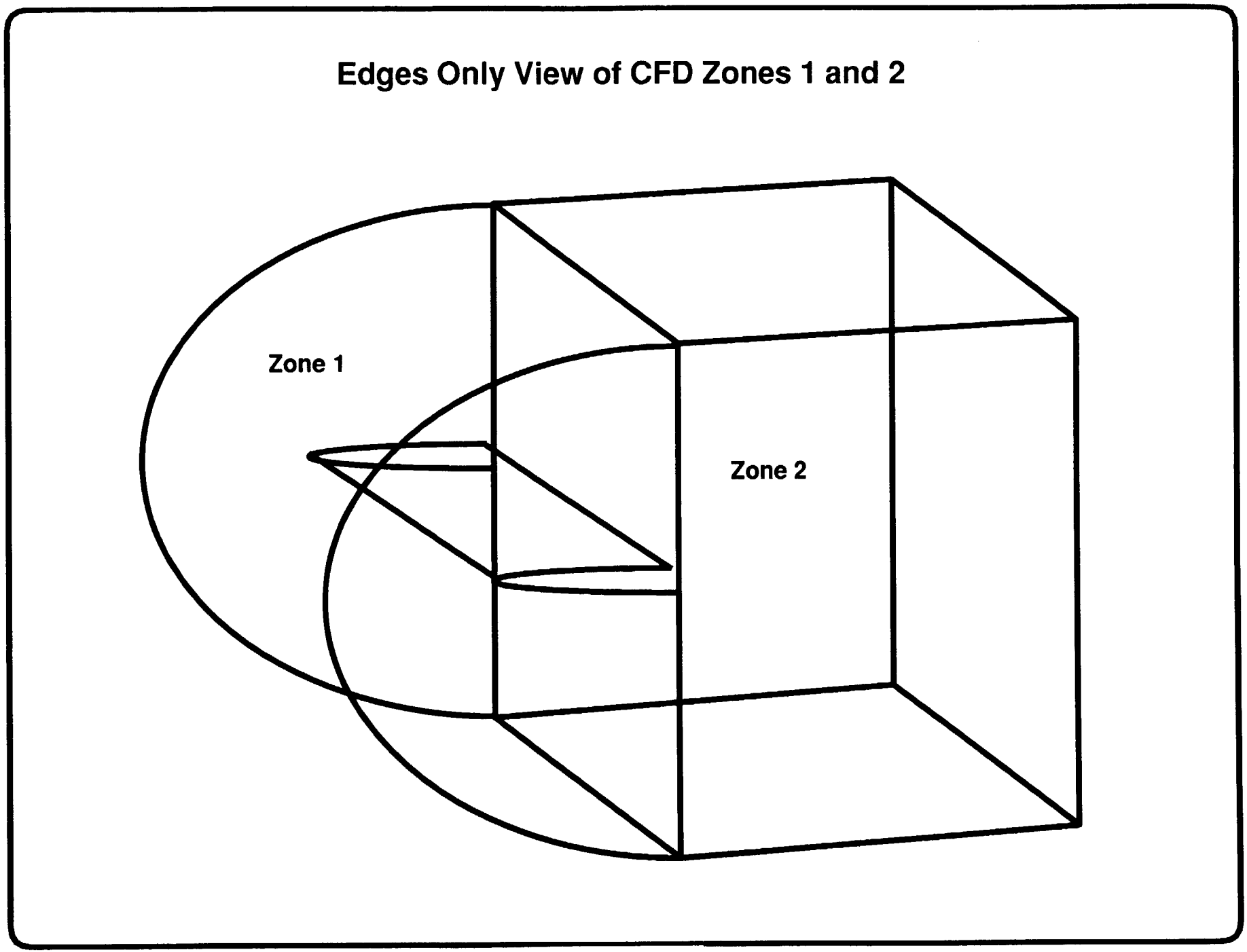

Figure 1

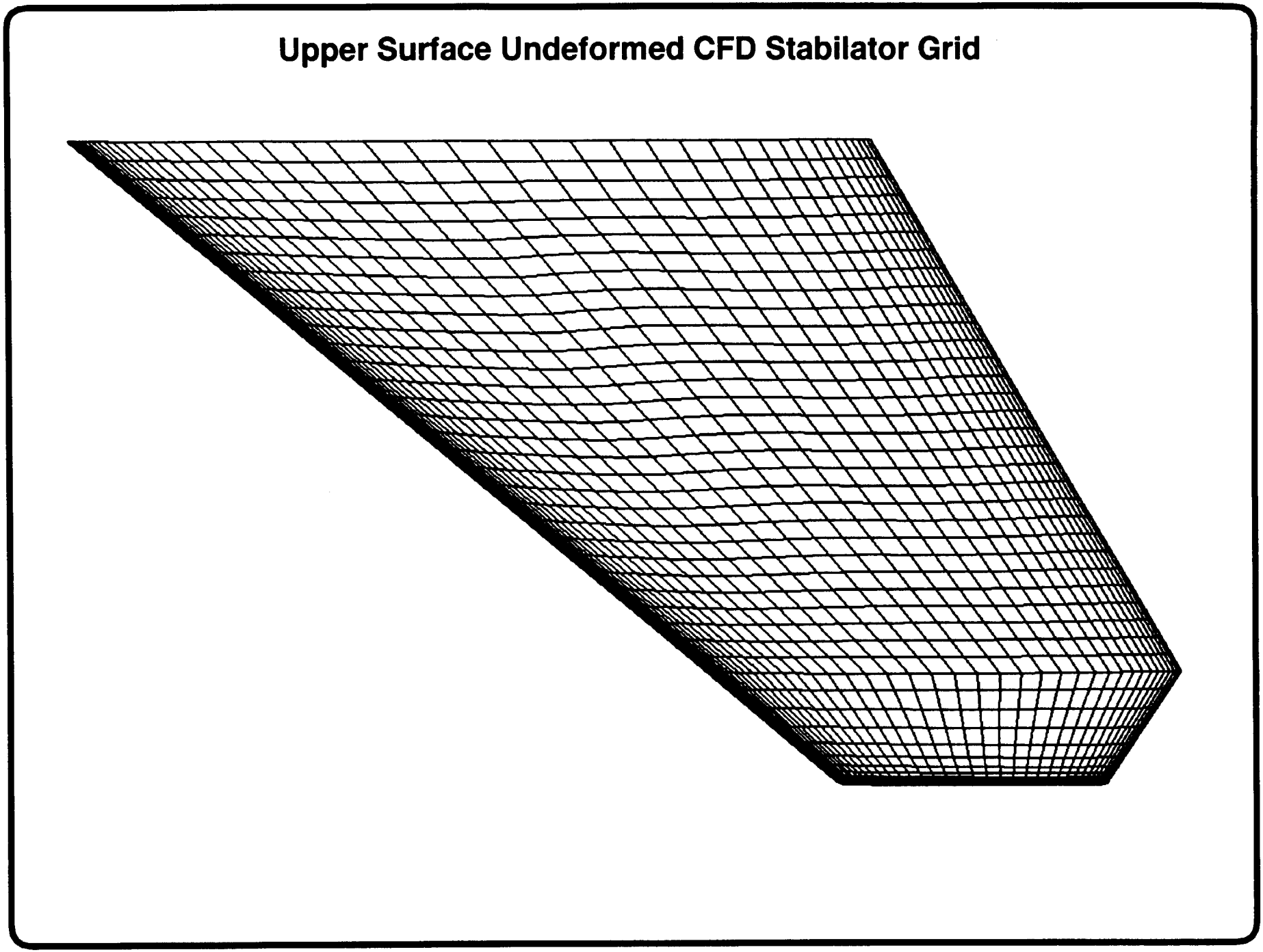

Figure 2

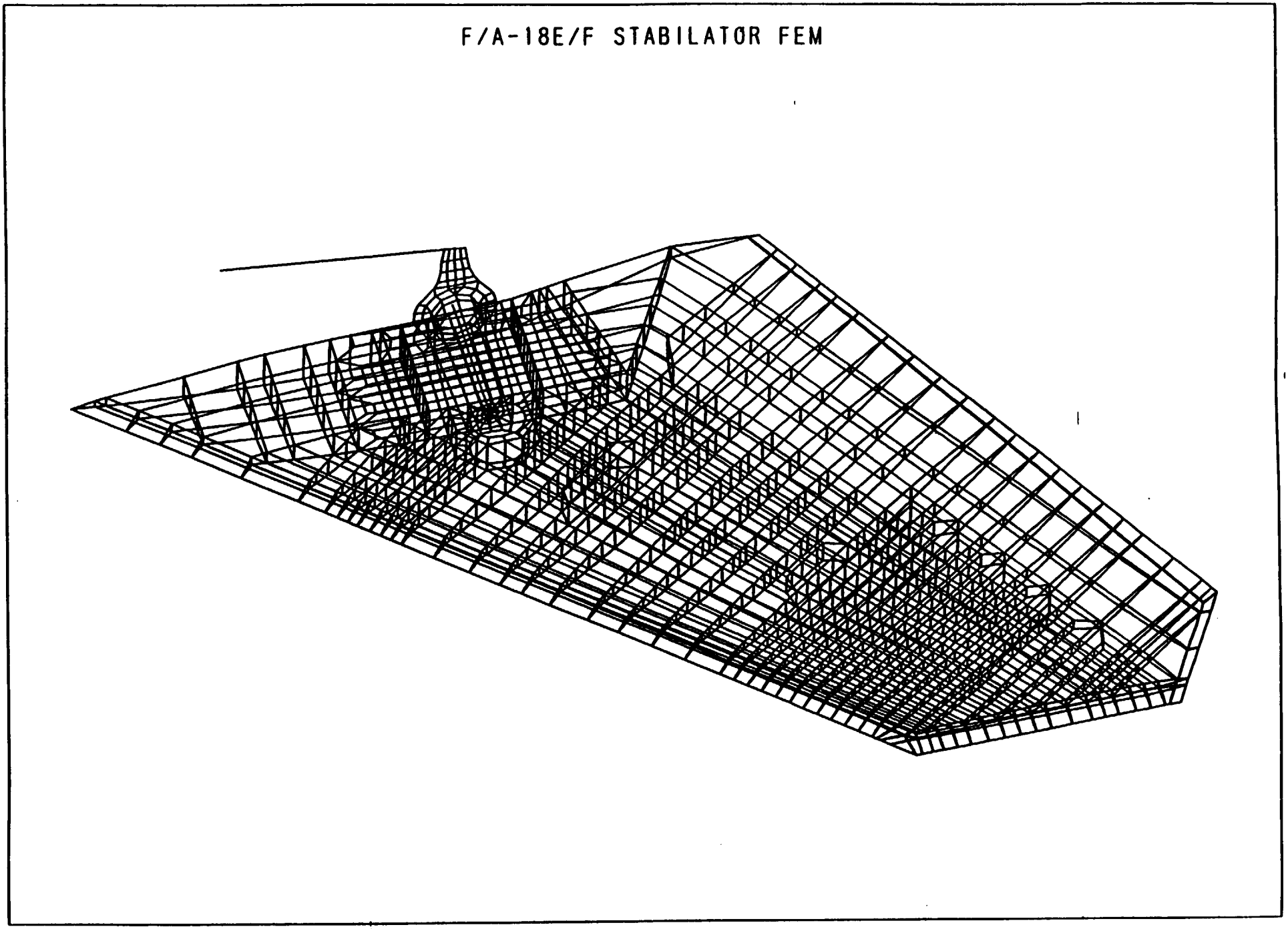

Figure 3

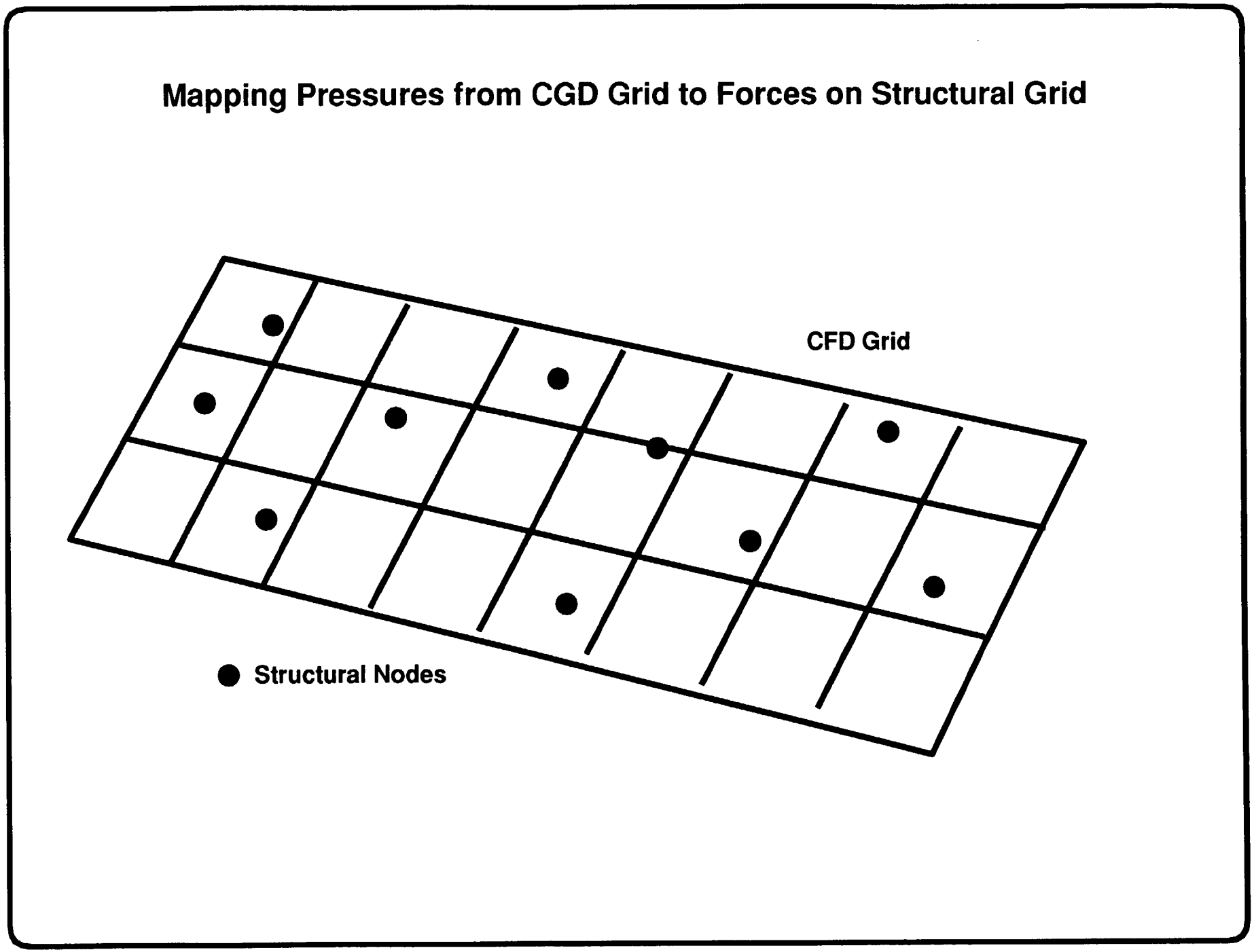
Mapping Pressures from CGD Grid to Forces on Structural Grid
CFD Grid
Structural Nodes

Figure 4

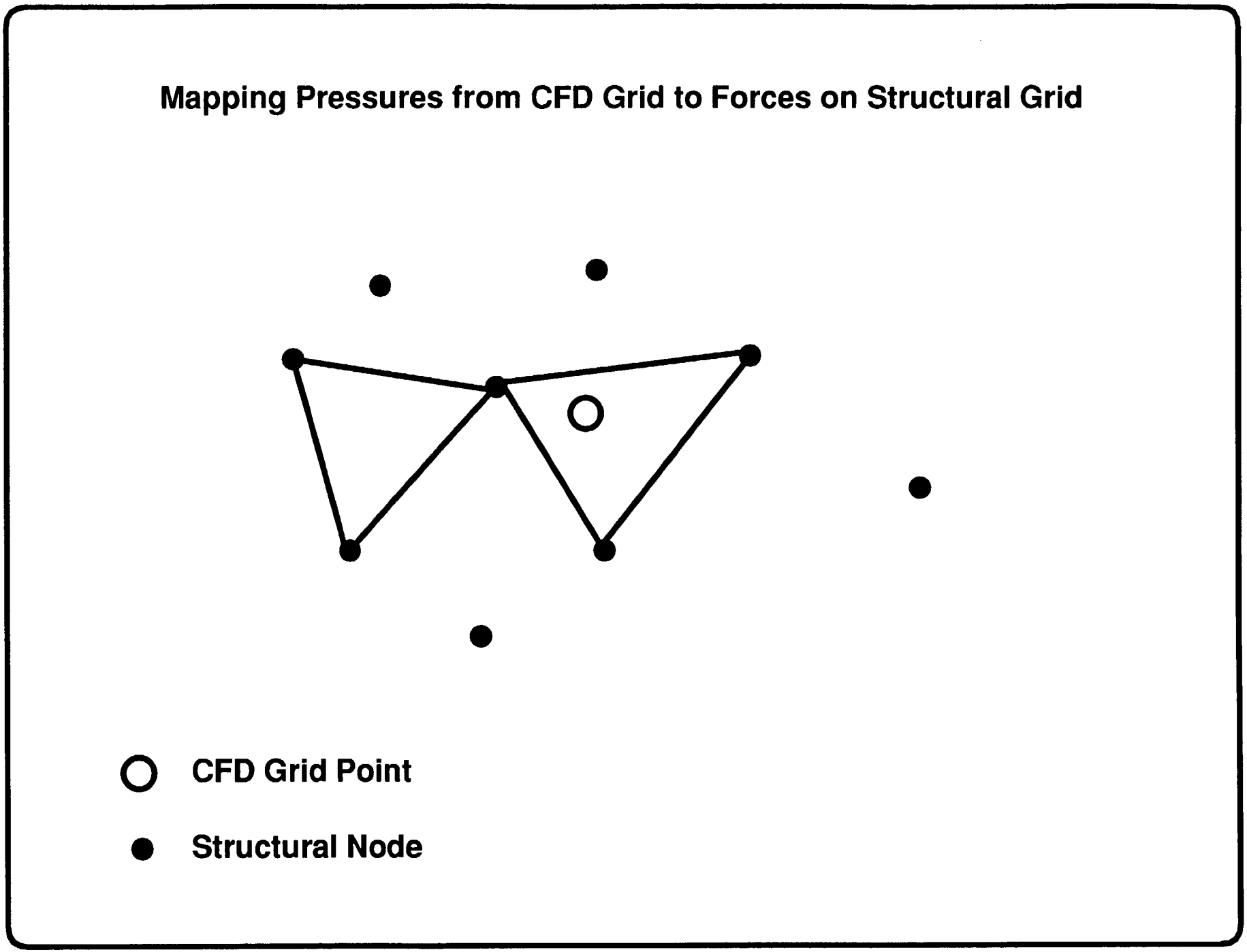
Mapping Pressures from CFD Grid to Forces on Structural Grid
CFD Grid Point
Structural Node

Figure 5

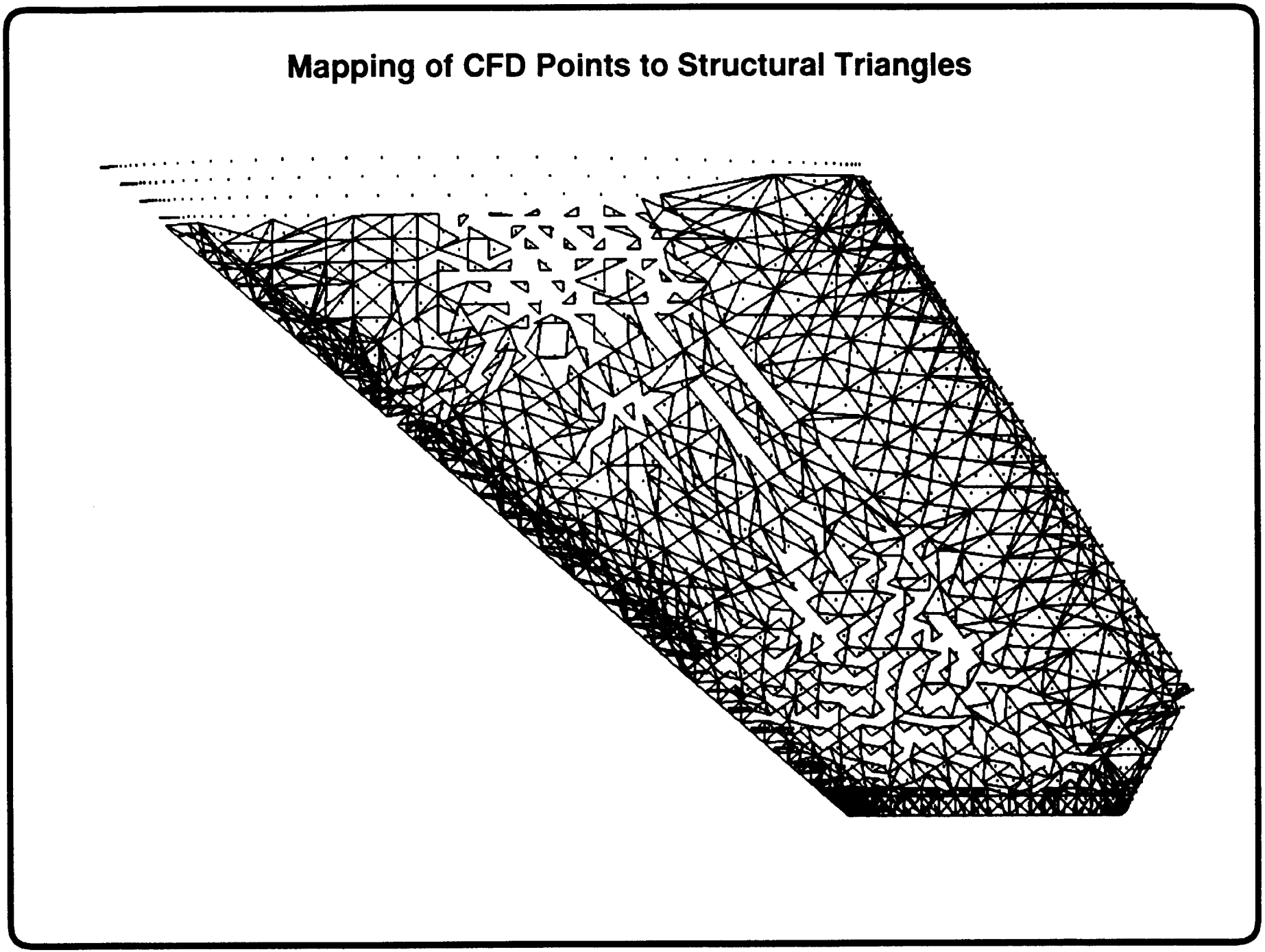

Figure 6

Surface Grid Used to Deform Interior Grid

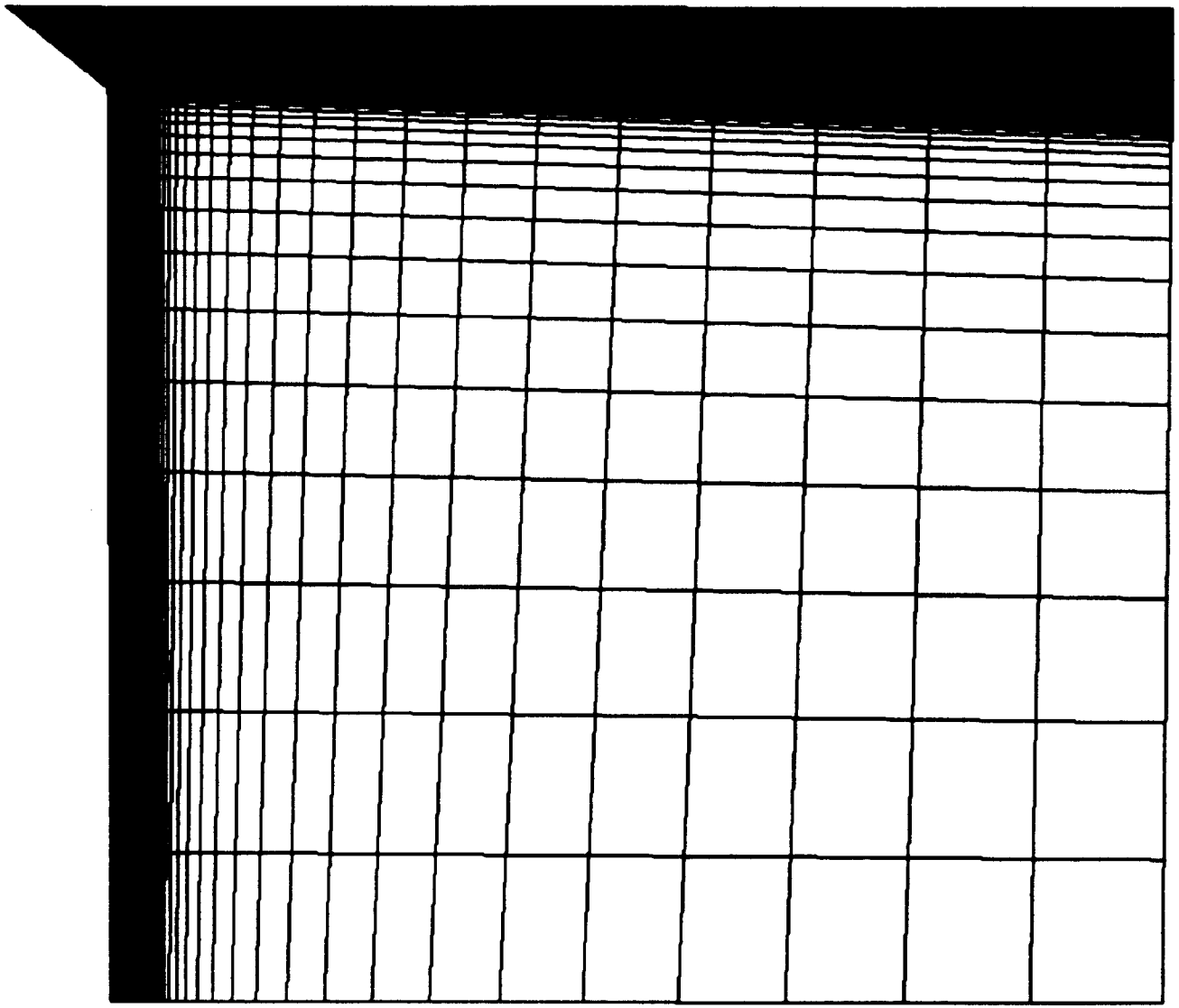

Figure 7

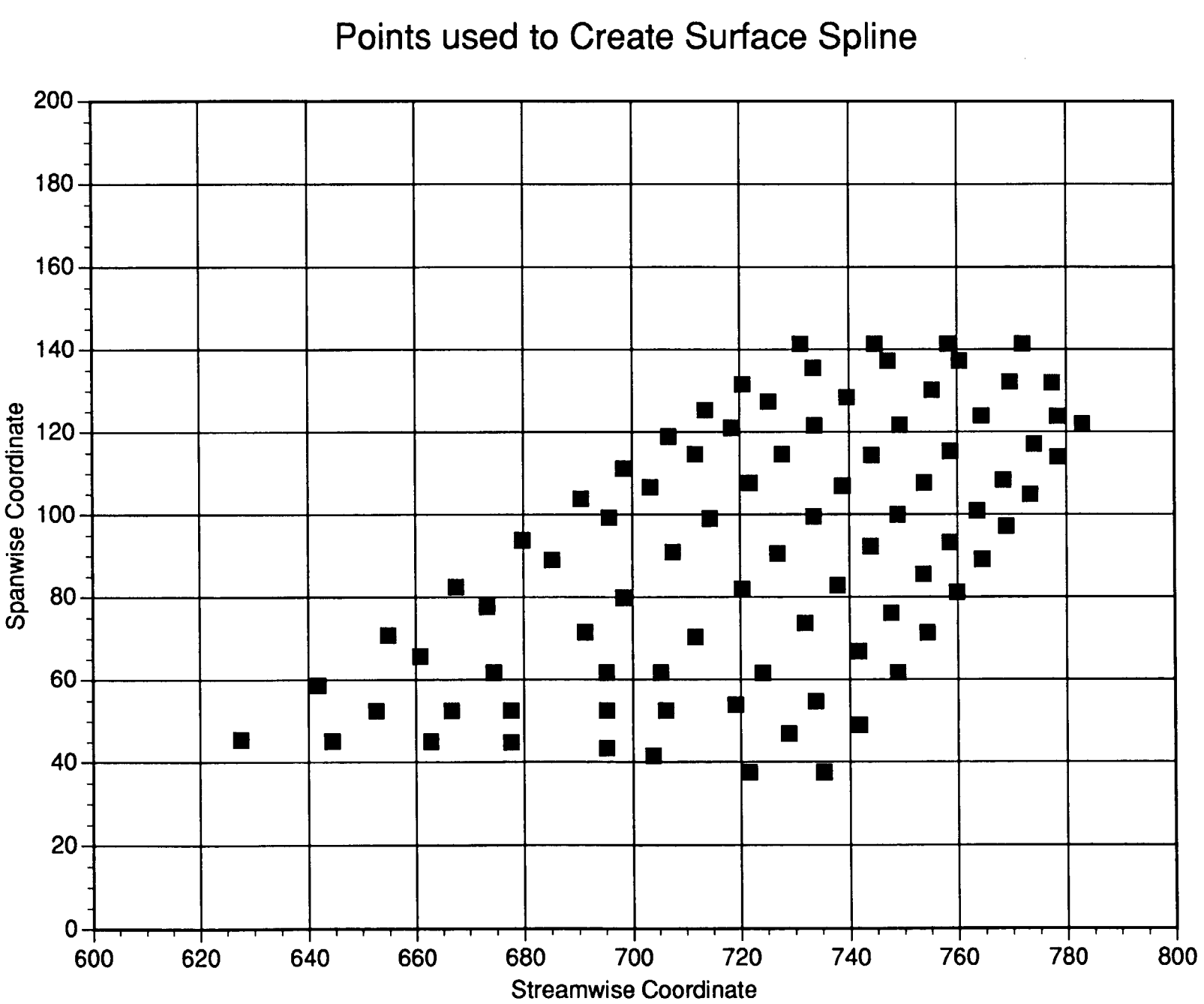
Points used to Create Surface Spline
Spanwise Coordinate
Streamwise Coordinate
0
20
40
60
80
100
120
140
160
180
200
600
620
640
660
680
700
720
740
760
780
800

Figure 8

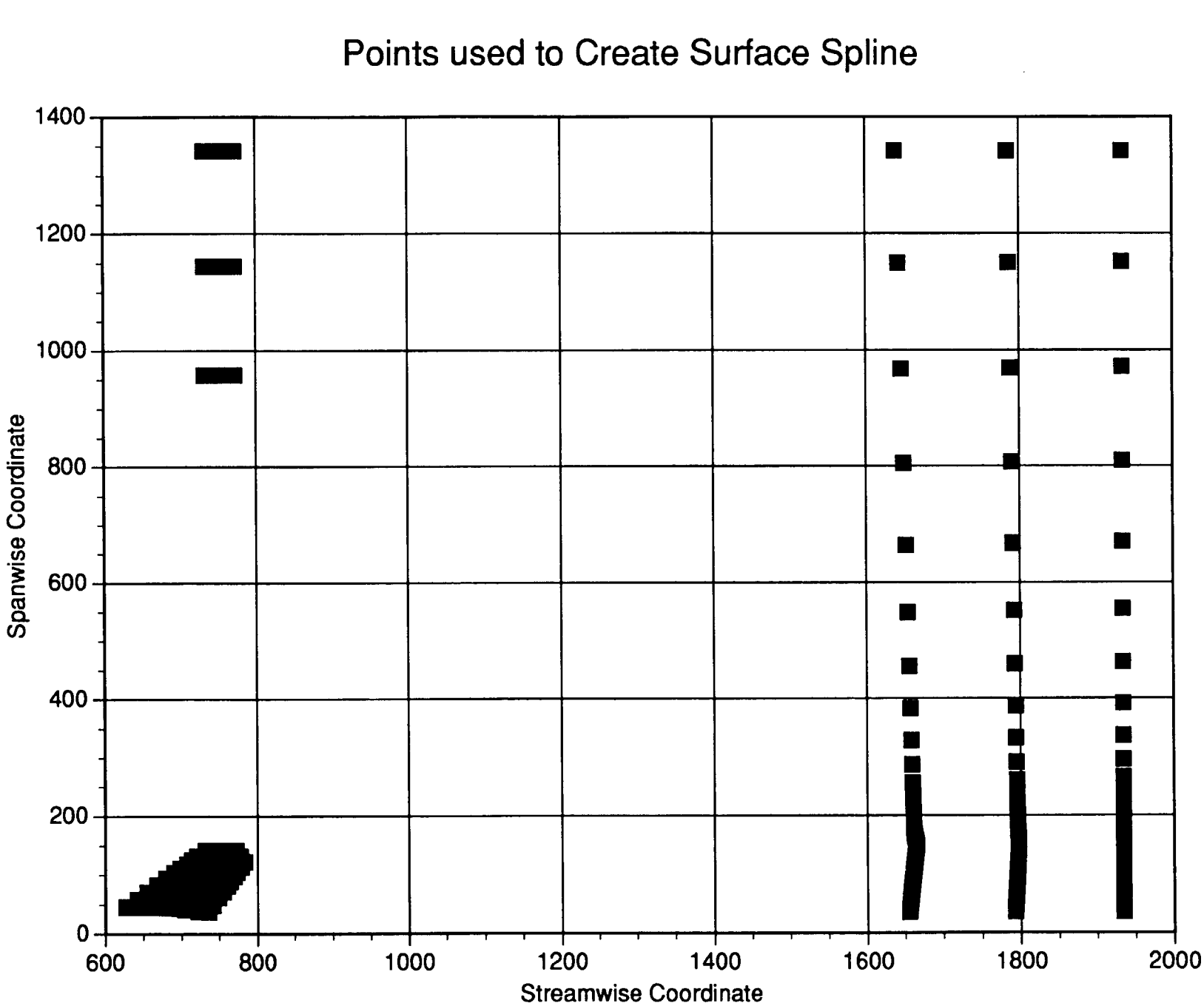
Points used to Create Surface Spline
Spanwise Coordinate
Streamwise Coordinate
0
200
400
600
800
1000
1200
1400
600
800
1000
1200
1400
1600
1800
2000

Figure 9

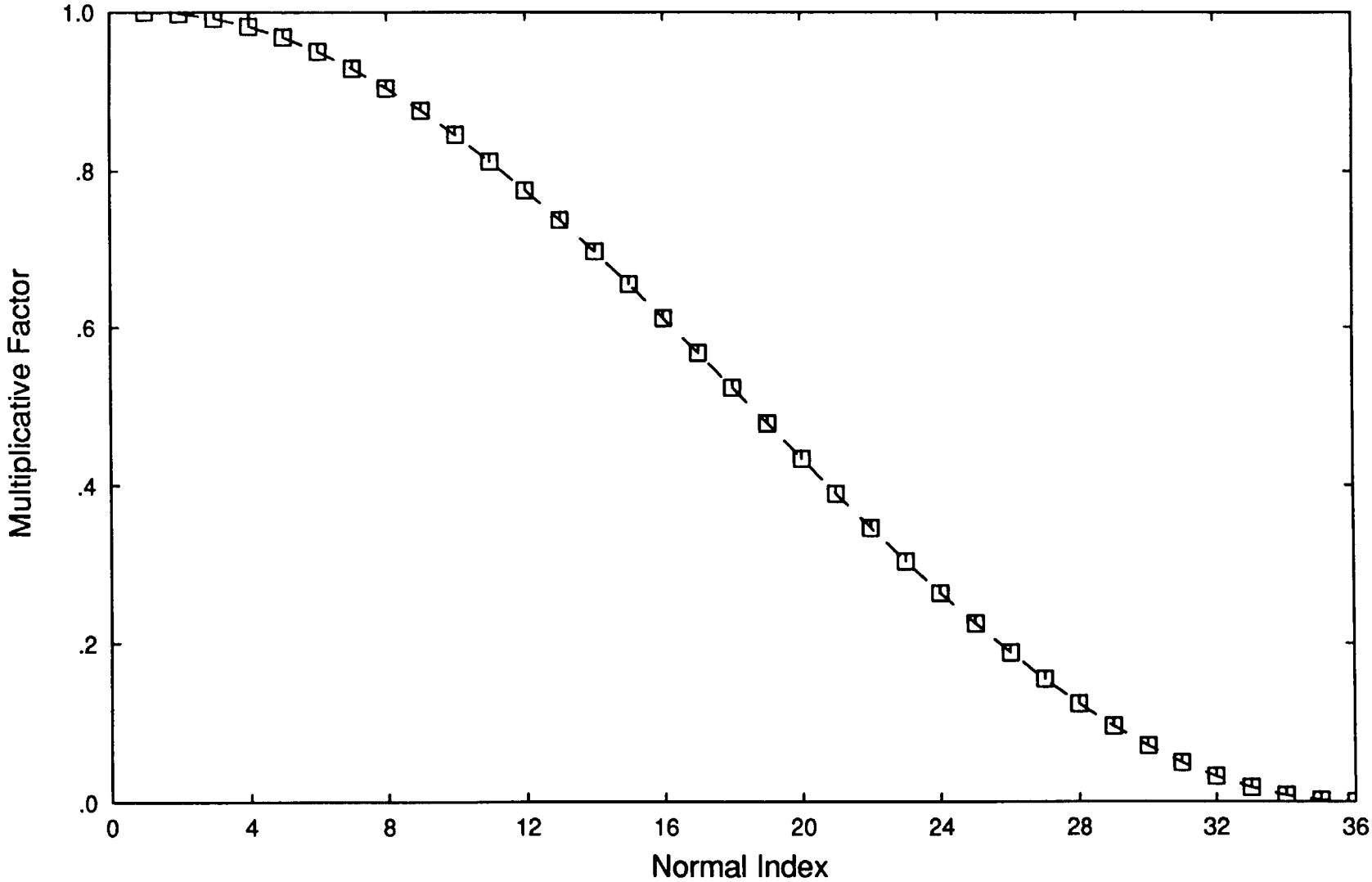
Cosine Spacing Function
Multiplicative Factor vs. Normal Index
Multiplicative Factor
1.0
.8
.6
.4
.2
.0
0
4
8
12
16
20
24
28
32
36
Normal Index

Figure 10

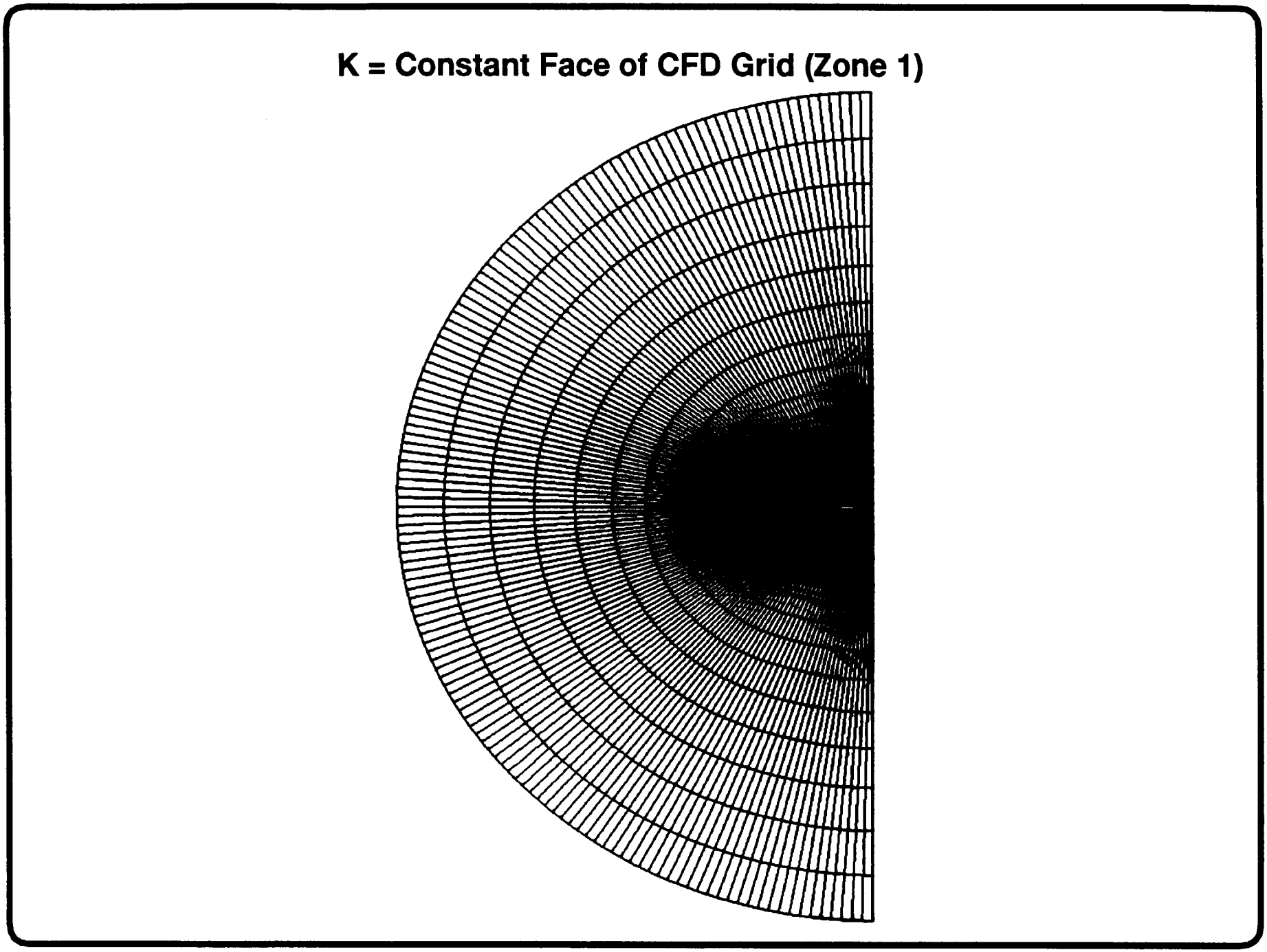

Figure 11

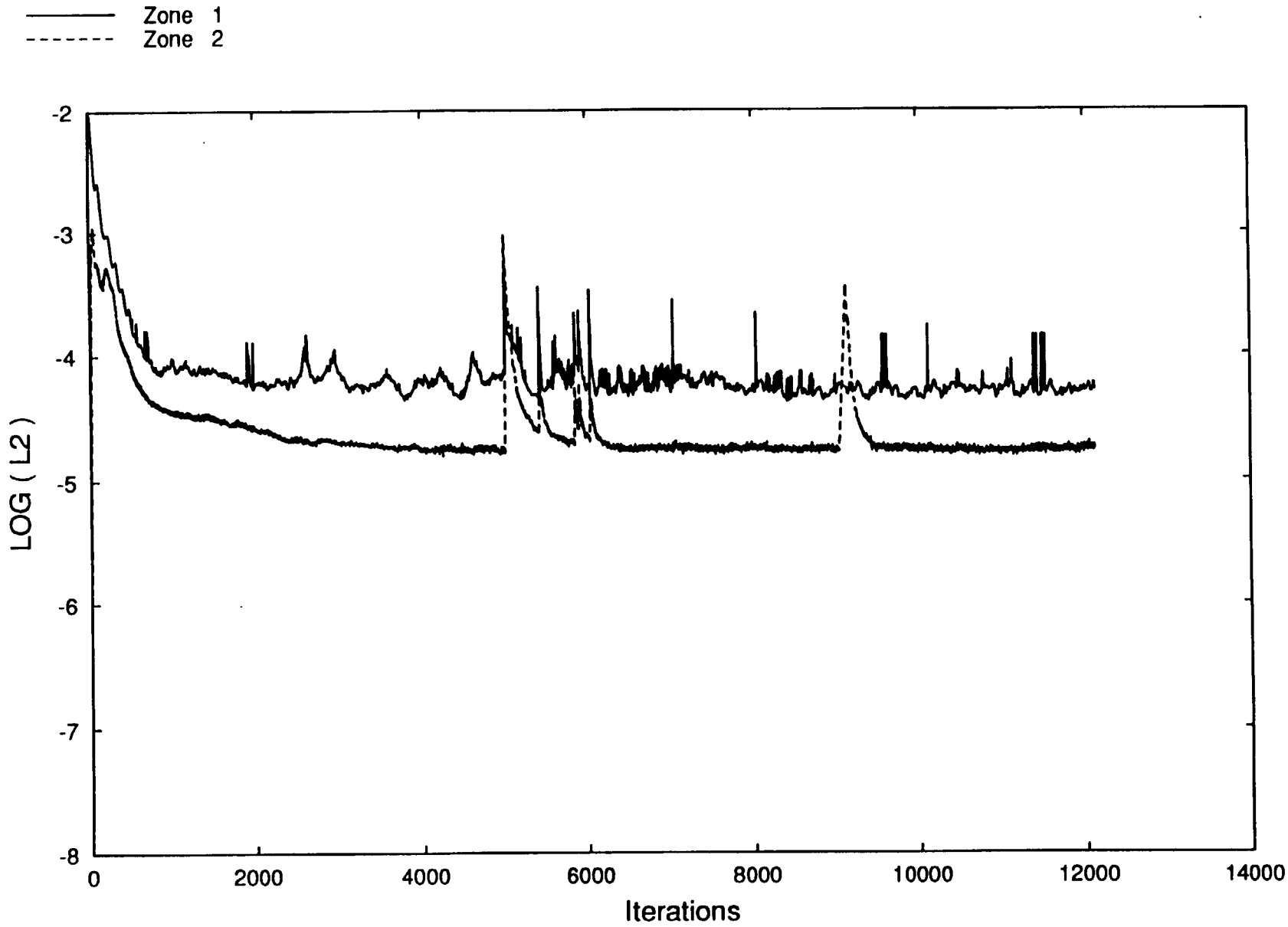
F/A-18 Horizontal Stabilator
Mach 0.95 Sea Level Static
Zone 1
Zone 2
-2
-3
-4
-5
-6
-7
-8
LOG (L2)
0
2000
4000
6000
8000
10000
12000
14000
Iterations

Figure 12

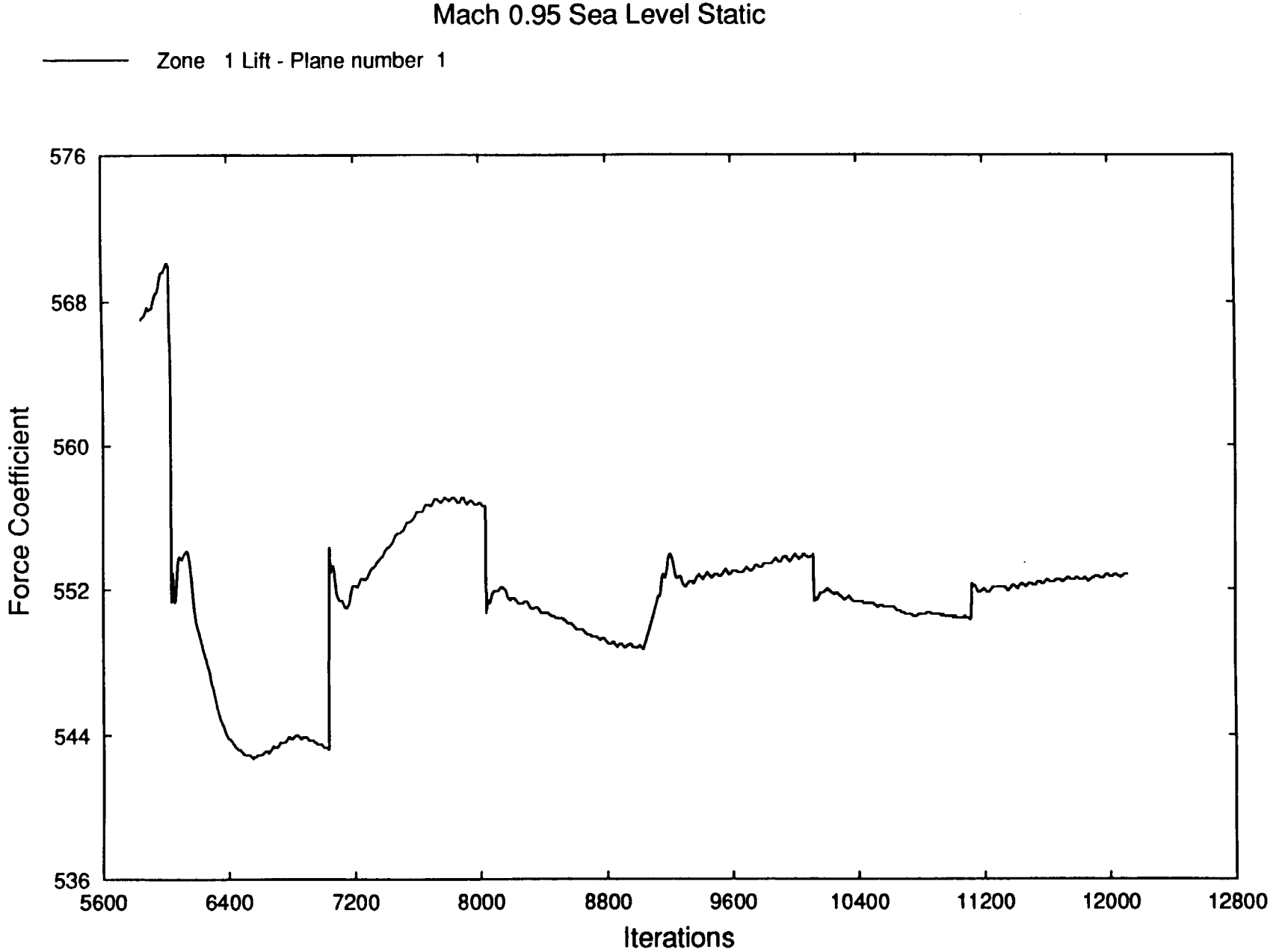
F/A-18 Horizontal Stabilator
Mach 0.95 Sea Level Static
Zone 1 Lift - Plane number 1
Force Coefficient
576
568
560
552
544
536
5600
6400
7200
8000
8800
9600
10400
11200
12000
12800
Iterations

Figure 13

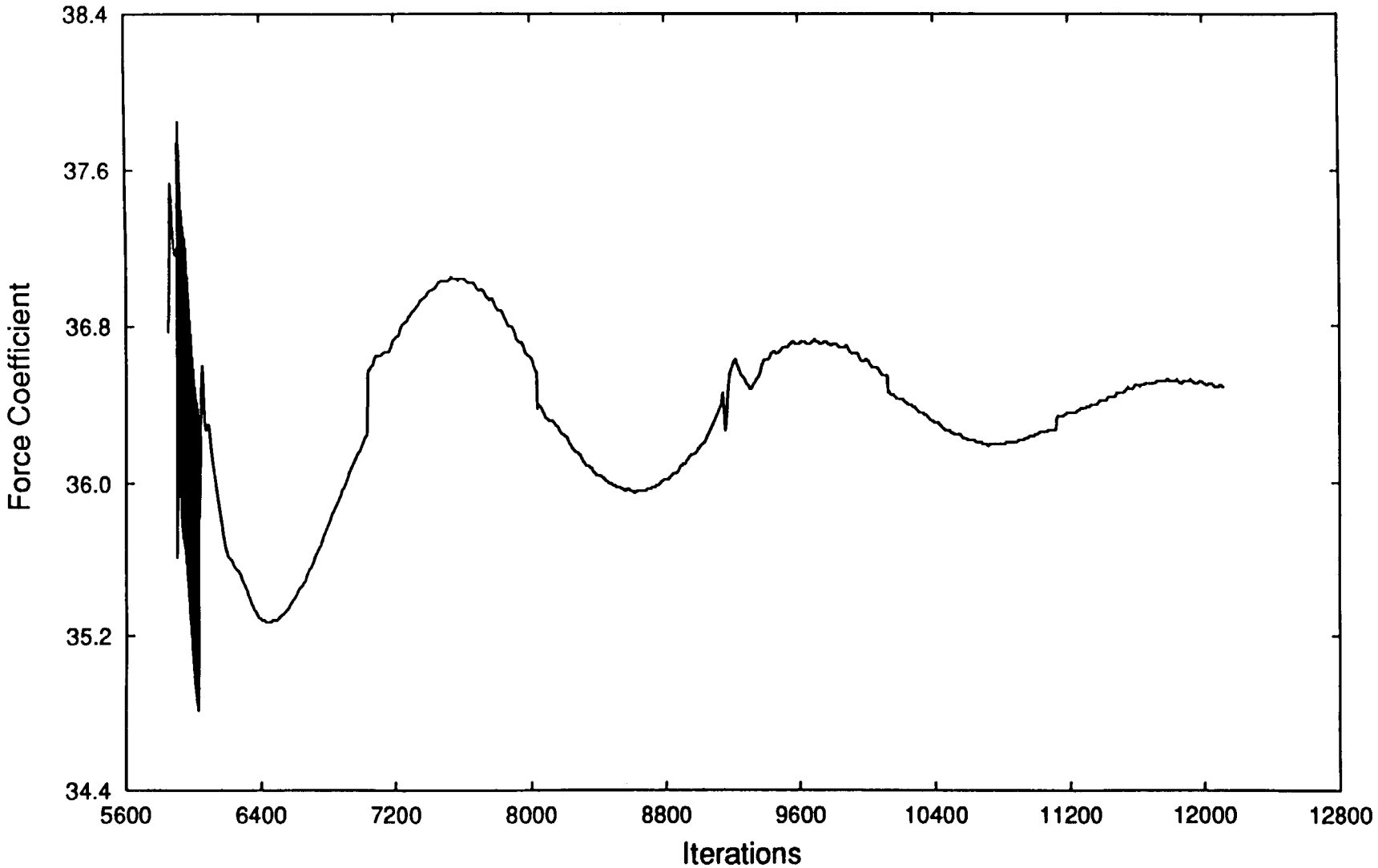
F/A-18 Horizontal Stabilator
Mach 0.95 Sea Level Static
Zone 1 Drag - Plane Number 1
Force Coefficient
38.4
37.6
36.8
36.0
35.2
34.4
5600
6400
7200
8000
8800
9600
10400
11200
12000
12800
Iterations

Figure 14

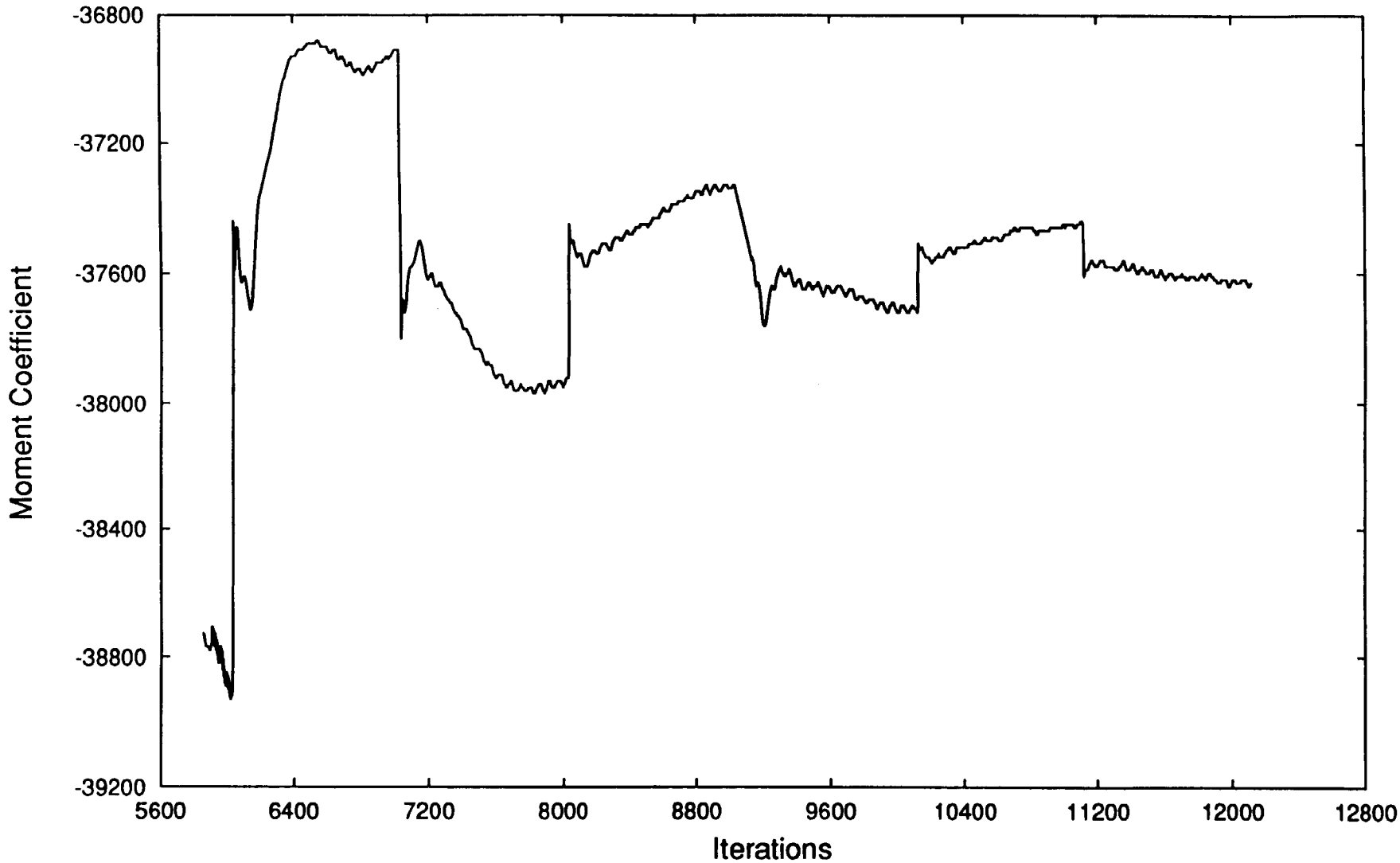
F/A-18 Horizontal Stabilator
Mach 0.95 Sea Level Static
Zone 1 X-Component - Plane Number 1
Moment Coefficient
-36800
-37200
-37600
-38000
-38400
-38800
-39200
5600
6400
7200
8000
8800
9600
10400
11200
12000
12800
Iterations

Figure 15

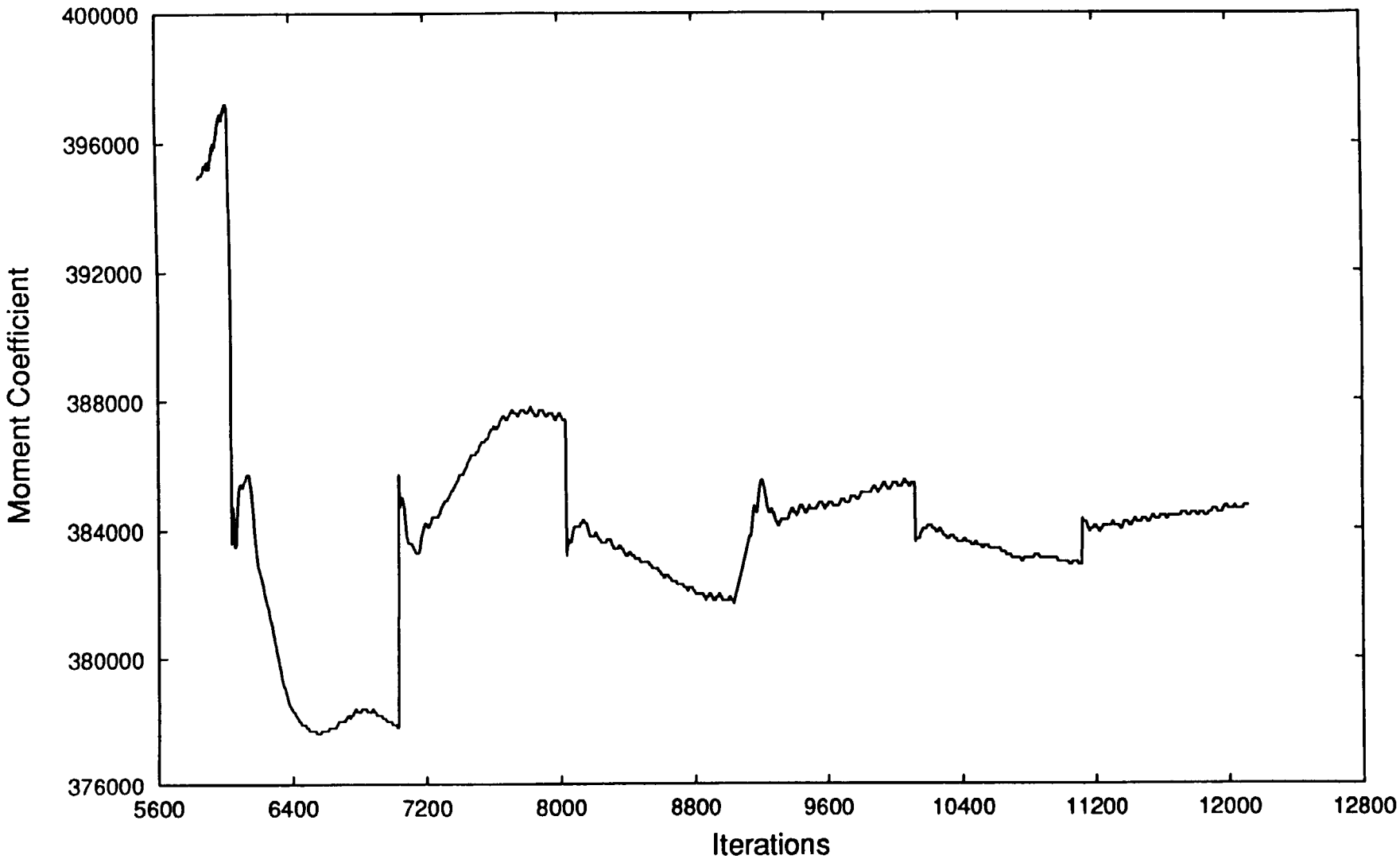
F/A-18 Horizontal Stabilator
Mach 0.95 Sea Level Static
Zone 1 Z-Component - Plane Number 1
Moment Coefficient
400000
396000
392000
388000
384000
380000
376000
5600
6400
7200
8000
8800
9600
10400
11200
12000
12800
Iterations

Figure 16

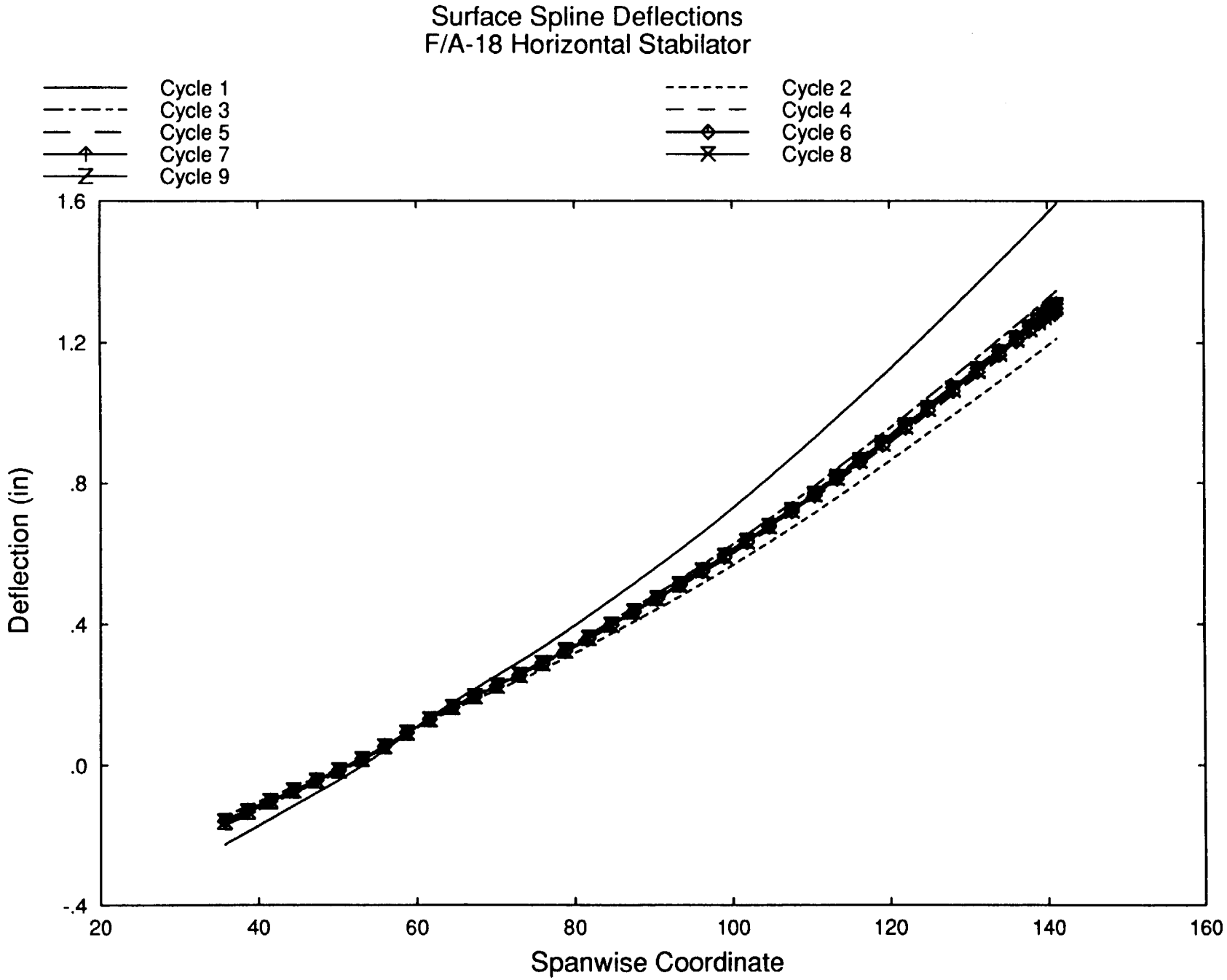
Surface Spline Deflections
F/A-18 Horizontal Stabilator
Cycle 1
Cycle 2
Cycle 3
Cycle 4
Cycle 5
Cycle 6
Cycle 7
Cycle 8
Cycle 9
1.6
1.2
.8
.4
.0
-.4
Deflection (in)
20
40
60
80
100
120
140
160
Spanwise Coordinate

Figure 17

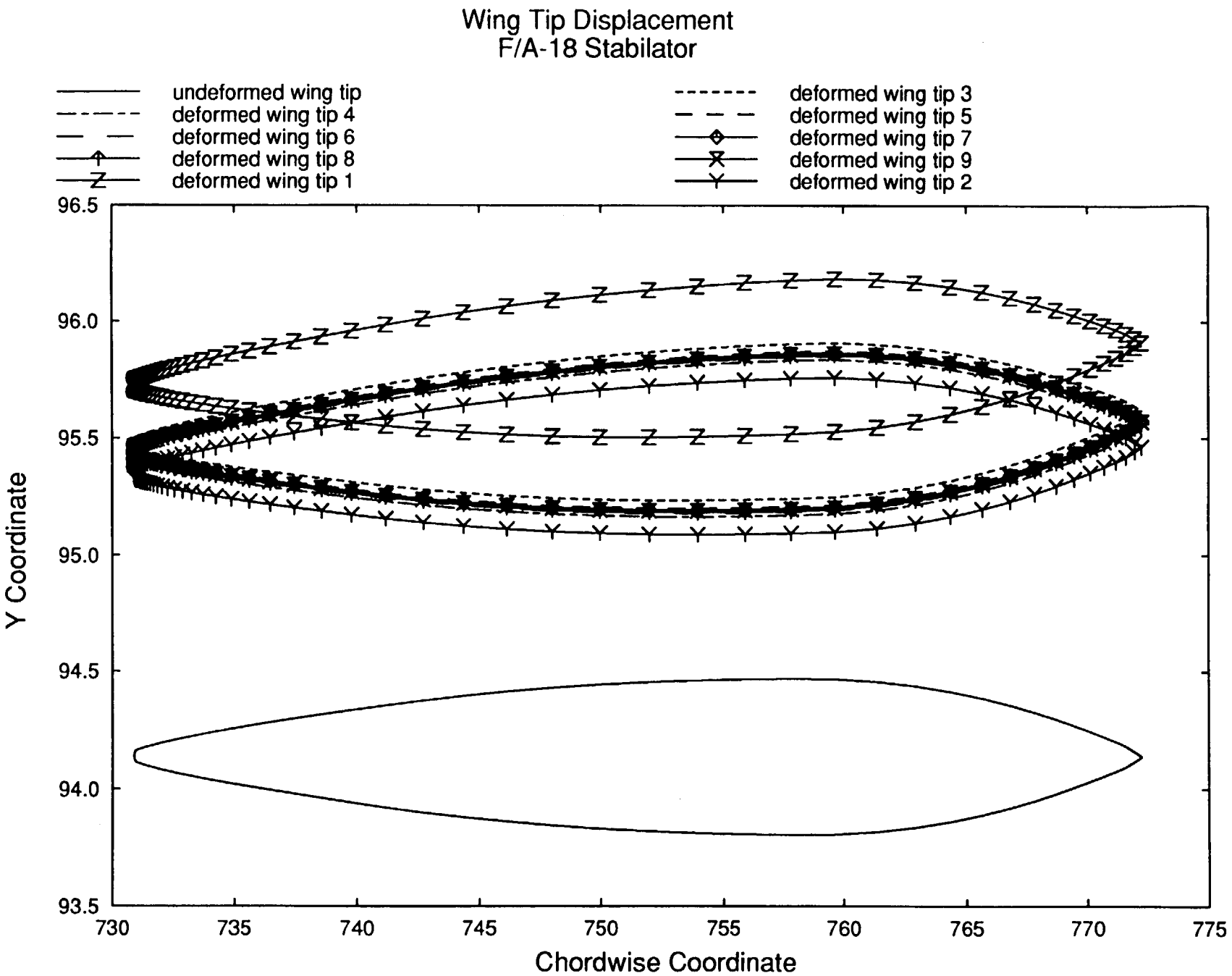
Wing Tip Displacement
F/A-18 Stabilator
undeformed wing tip
deformed wing tip 4
deformed wing tip 6
deformed wing tip 8
deformed wing tip 1
deformed wing tip 3
deformed wing tip 5
deformed wing tip 7
deformed wing tip 9
deformed wing tip 2
96.5
96.0
95.5
95.0
94.5
94.0
93.5
Y Coordinate
730
735
740
745
750
755
760
765
770
775
Chordwise Coordinate

Figure 18

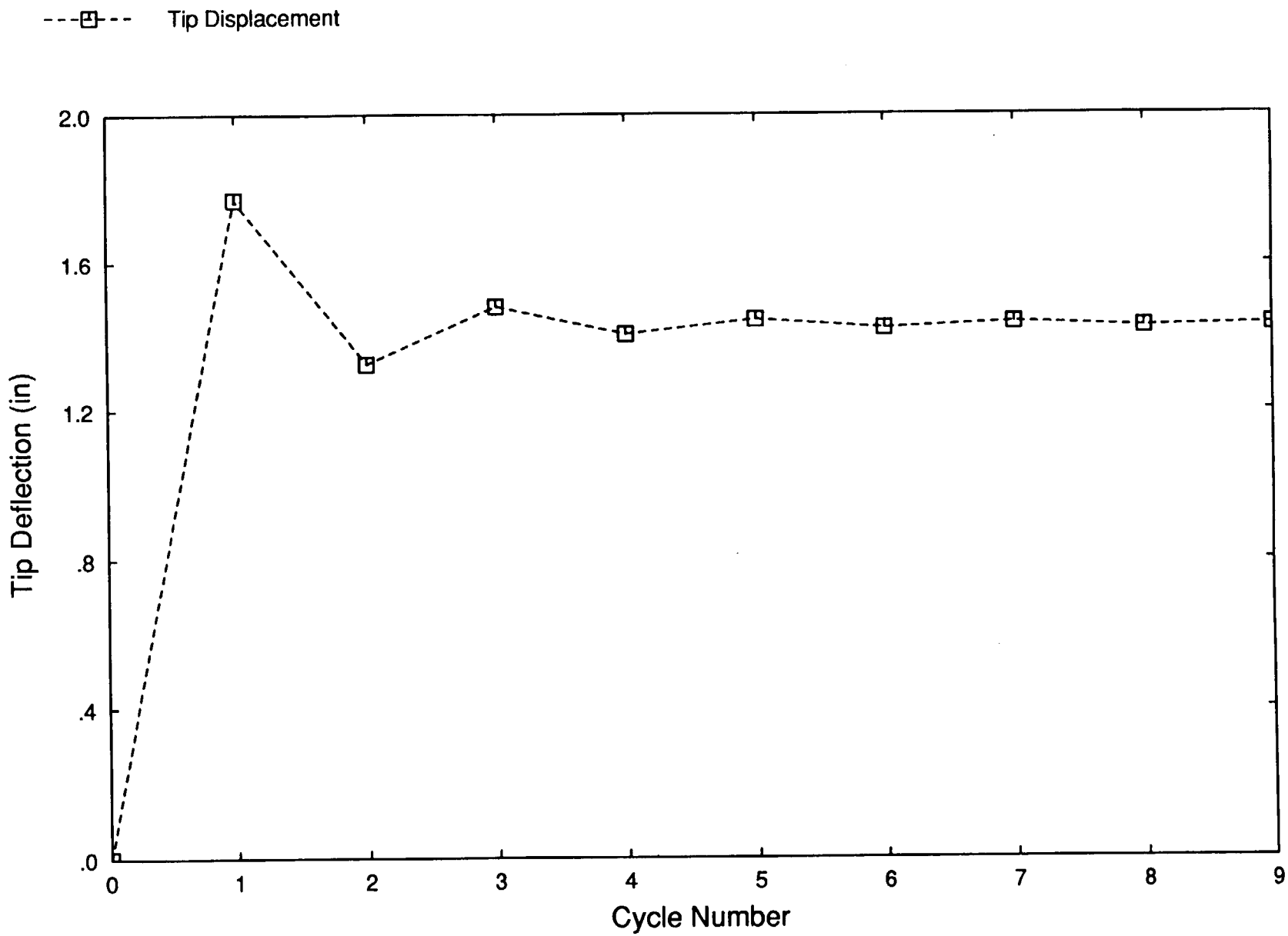
Wing Tip Displacement
F/A-18 Stabilator
Tip Displacement
Tip Deflection (in)
2.0
1.6
1.2
.8
.4
.0
0
1
2
3
4
5
6
7
8
9
Cycle Number

Figure 19

Deformed and Undeformed Upper Surface of Stabilator

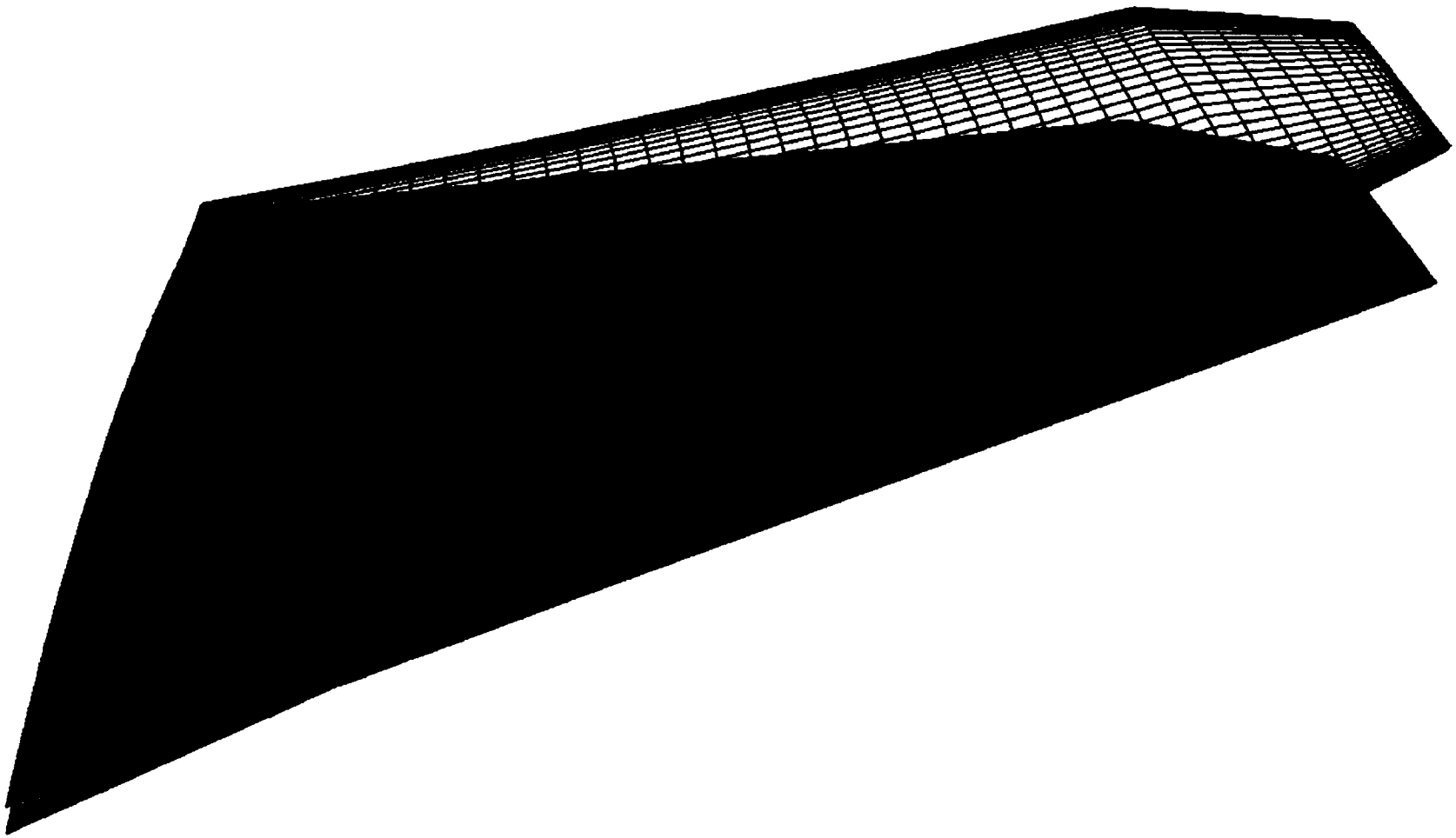

Deflections scaled by a factor of 10

Figure 20

Pressure Coefficient Variation of Rigid vs Flexible Stabilator

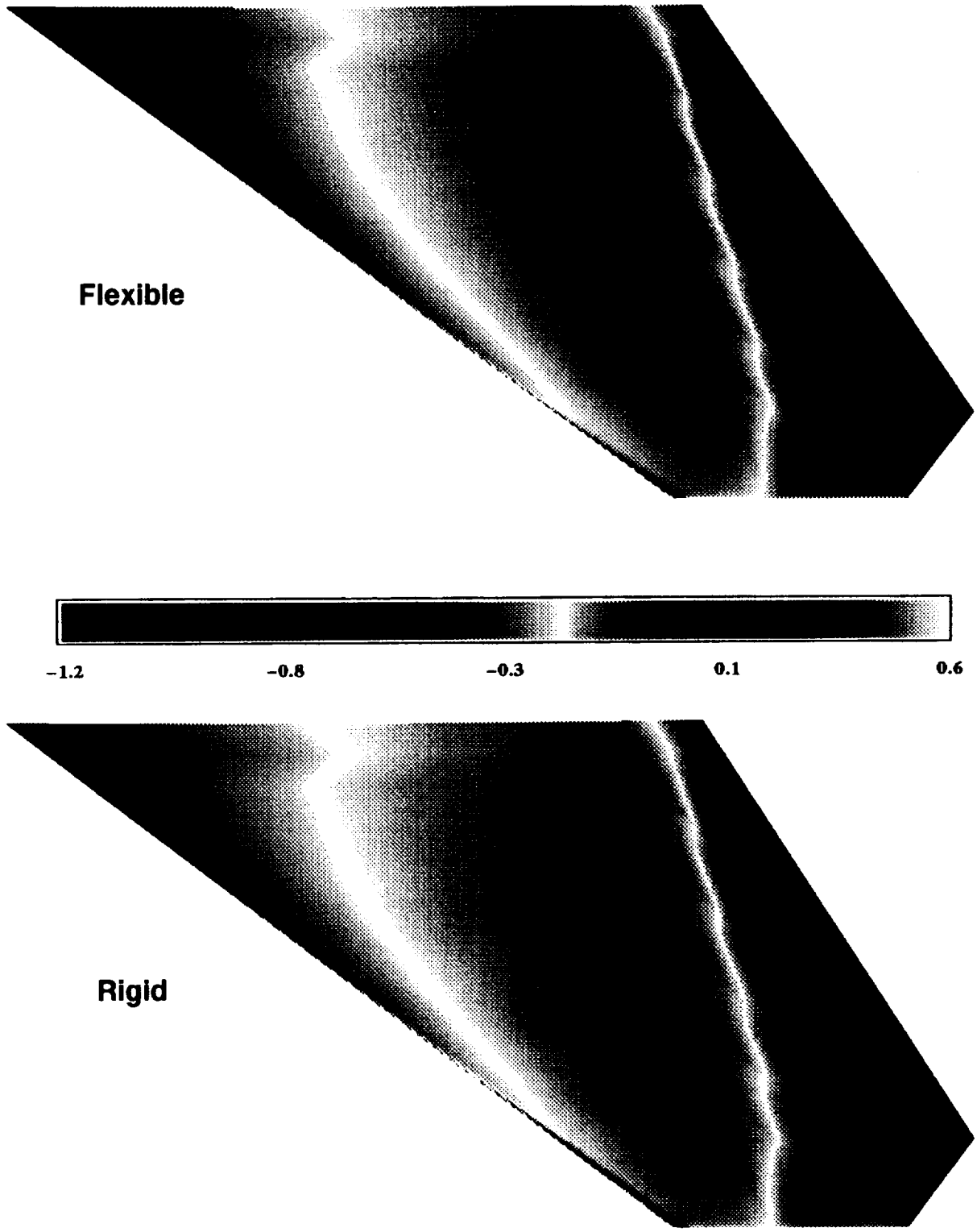

Figure 21

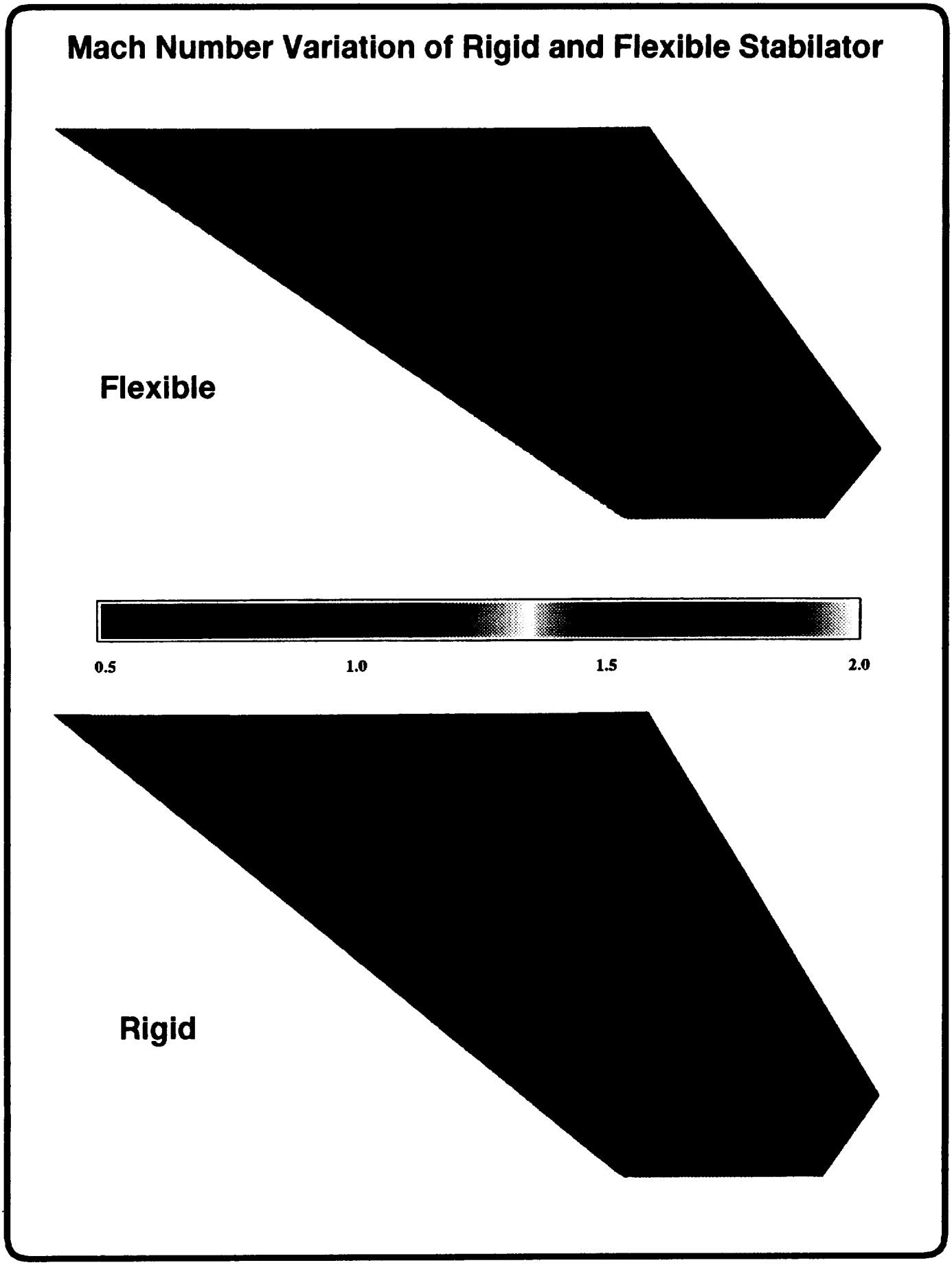
Mach Number Variation of Rigid and Flexible Stabilator
Flexible
0.5
1.0
1.5
2.0
Rigid

Figure 22